



ELSEVIER

Surface Science 327 (1995) 145–164

surface science

Glancing-angle X-ray scattering studies of the premelting of ice surfaces

H. Dosch^{a,b,*}, A. Lied^{a,c}, J.H. Bilgram^d

^a *Sektion Physik der Universität München, D-80539 München, Germany*

^b *Institut für Materialwissenschaften der Bergischen Universität Gesamthochschule Wuppertal, D-42285 Wuppertal, Germany*

^c *Institut Laue Langevin, P.O. Box 156 X, F-38042 Grenoble, Cedex, France*

^d *Labor für Festkörperphysik der ETH-Hönggerberg, CH-8093 Zürich, Switzerland*

Received 14 October 1994; accepted 28 November 1994

Abstract

The onset of surface melting at {00.1} (“basal”), {10.0} and {11.0} (“nonbasal”) surfaces of hexagonal ice is studied experimentally by glancing-angle X-ray scattering. The preparation of mirror-like single crystal ice surfaces and a special in situ X-ray chamber is described in detail. The X-ray scattering experiments using synchrotron radiation give clear evidence that all the investigated high-symmetry surfaces exhibit surface melting with onset temperatures $T_s \cong -13.5^\circ\text{C}$ for the basal and $T_s \cong -12.5^\circ\text{C}$ for the nonbasal surfaces. The temperature dependence of the thickness of the quasiliquid is presented and discussed in view of various theoretical predictions. In addition we found thermal faceting at nonbasal surfaces as well as a diffuse (“rough”) solid-quasiliquid interface. The thermal properties of the observed surface disorder implies that the correlation length within the so-called “surface melt” is much larger than the correlation length in the bulk liquid indicating the presence of significant “substrate” interactions.

Keywords: Solid–liquid interfaces; Surface melting; Surface structure; Vicinal single crystal surfaces; Water; Wetting; X-ray scattering

1. Introduction

Melting is considered to be the most ubiquitous phase transition in matter. In view of the importance of melting in technology and in our everyday life, it appears quite surprising that up to now there exists no accepted microscopic theory of melting. This lack of understanding of the possible microscopic mechanisms which lead to the melting of a solid has its origin in the still very incomplete knowledge of the

structure of liquids and in the general complications associated with first order phase transitions. In the last years the role of surfaces and interfaces as possible two-dimensional nucleation sites for the liquid phase reappeared in the focus of scientific interest: There is a growing experimental evidence that the truncation of the 3-dimensional translational invariance at the surface favours the transition to the disordered liquid state already at temperatures well below the bulk melting point (T_m). This phenomenon is commonly called surface melting which sets in at the so-called onset temperature T_s . In the regime of surface melting, i.e., for $T_s \leq T < T_m$, a sheet of a

* Corresponding author.

disordered surface layer appears which grows in thickness upon approaching T_m .

A particularly exciting case is the surface melting of ice. It is argued that an eventually present quasiliquid surface layer on ice well below the actual melting point would affect many environmental processes which control our biosphere, as the motion of glaciers, the charging of thunderstorms, the growth of ice and frost heave [1]. Interestingly the concept of a surface melt has been coined by Faraday in 1859 [2] who attributed the ice regelation phenomenon to the presence of a microscopic liquid surface layer. Since then many experimental efforts have been undertaken in order to directly observe the surface melting of ice, however, due to the apparent difficulties to perform reproducible experiments on well-defined single crystal surfaces of ice, the current picture of the structure of ice surfaces close to melting is rather confusing and controversial. In this experimental study of ice surfaces we present surface-sensitive X-ray scattering experiments which have carefully been checked for reversibility with temperature and for reproducibility from sample to sample [3]. The obtained results give a clear evidence for the existence of a surface sheet with no crystal order well below 0°C .

This article is organized as follows: In Section 2 we shortly summarize the current understanding of the structure of ice surface close to the bulk melting point followed by a short discussion of the concepts of glancing angle X-ray scattering within the framework of the distorted wave Born approximation (DWBA), thereby introducing the relevant parameters which describe the contributions to surface disorder (Section 3). A detailed description of the sample preparation procedure and of the special in situ X-ray chamber is presented in Section 4, afterwards, in Section 5, the actual X-ray experiments and the experimental results are shown and shortly commented. The quantitative analysis and the discussion of the obtained results is found in Section 6.

2. Structure, melting and surface melting of Ih ice

At ambient pressure H_2O crystallizes at $T = 0^\circ\text{C}$ in the hexagonal crystal structure with the symmetry element $P6_3/\text{mmc}$, commonly denoted as Ih ice.

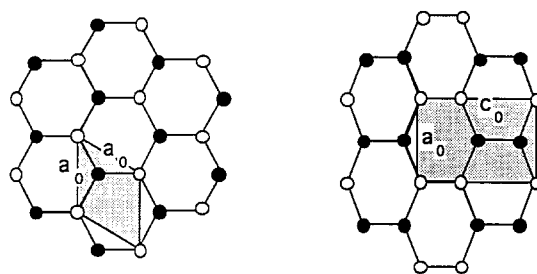


Fig. 1. Ih ice structure of the basal plane (left) and the prism plane (right). $a_0 = 4.52 \text{ \AA}$ and $c_0 = 7.36 \text{ \AA}$ are the lattice parameters associated with the hexagonal unit cell. The full symbols show the outermost atoms, the open symbols the atoms of the second layer.

Fig. 1 depicts the molecular arrangements of the basal and prism plane with the associated lattice parameters $a_0 = 4.52 \text{ \AA}$ and $c_0 = 7.36 \text{ \AA}$. In the following we will use the Miller index notation (hk.l) with h and k as the two nonorthogonal directions within the basal plane and l as the perpendicular direction. The structure of ice is mediated by a very efficient hydrogen bonding network. Its stability is reflected in the relatively large values of the heat of sublimation, $\lambda_s = 0.53 \text{ eV/molecule}$, and the latent heat of melting, $\lambda_m = 62 \text{ meV/molecule}$. Upon melting the crystalline long range order disappears and a liquid short range order emerges, governed by the (bulk) correlation length $\xi_b \cong 8 \text{ \AA}$ [4].

One of the earliest quantitative theories predicting surface melting of ice (after the original suggestion by Faraday) has been provided by Fletcher [5] who calculated the gain in free energy, if a disordered quasiliquid surface layer would allow for a more favorable reorientation of the polar water molecules. Though the onset of this ice surface melting scenario depends on the assumption on the details of the underlying interactions, one essentially arrives at a temperature dependent thickness L_d of the surface melt which can be cast into the form [6]

$$L_d = (11 \pm 4 \text{ \AA}) \ln \left| \frac{T_s}{T_m - T} \right|, \quad (1)$$

with an onset temperature of $T_s \leq -6.5^\circ\text{C}$ (also depending on the strength of the interactions). Experimental evidence for the existence of a quasiliquid surface layer in ice below 0°C has been obtained with the help of various techniques ranging from careful measurements of the velocity of a wire mov-

ing through ice [7], measurements of adhesion and friction of ice in contact with matter [8] to measurements of the electrical surface conductivity [9] and of the photoemission of ice [10]. When surface melting of ice is discussed one often is referring to two experimental efforts, the ion scattering experiments by Golecki and Jaccard [11] and the ellipsometry measurements by Beaglehole and Nason [12] and later by Furukawa [13]. Both experimental approaches seemingly provide a rather contradictory surface melting scenario: Evidence for a surface sheet with strong local disorder appearing at $T_s = -54^\circ\text{C}$ is found by ion scattering. At $T = -10^\circ\text{C}$ the thickness of this disorder has increased to $L_d \cong 400 \text{ \AA}$. Ellipsometry measurements at $\{00.1\}$ (“basal”) and $\{10.0\}$ (“prism”) ice surfaces, on the other hand, disclose a change of the average index of refraction not before -2°C and -5°C , respectively, which has been referred to the formation of a quasiliquid surface layer. To add to the puzzle, recent interference microscopy experiments on ice sur-

faces show a rounding of prism facets at -1.5°C with signatures of a roughening transition [14]. The equilibrium shape of growing ice crystals which has been investigated in some detail [15,16] exhibits no more optically visible facets for $T \geq -10^\circ\text{C}$, an experimental fact which may be considered as a roughening transition [16], but which could as well indicate the appearance of an appreciable liquid surface layer which causes a noticeable rounding of the crystal shape.

An apparent drawback of all the experimental techniques applied so far to study ice surfaces close to the melting point is the fact that they do not couple to a relevant order parameter of the melting process. As one knows the most striking microscopic feature which accompanies melting is the disappearance of the long ranged crystal structure, i.e. the disappearance of the sharp Bragg reflections. Thus, when surface melting occurs, a surface sheet with no Bragg signal is expected to emerge. The experimental challenge is to set up a surface-sensitive scattering experiment which allows an unambiguous detection of this surface melting signature. This will be described in what follows [3,17].

3. Elements of glancing-angle X-ray scattering

In order to observe a quasiliquid surface layer on ice we applied the scheme of glancing angle X-ray scattering (GAXS) [18,19] which appears as an almost ideal experimental technique for the application to ice surfaces for several reasons as:

(a) Unlike low-energy electron diffraction (LEED) or ion scattering techniques (LEIS) GAXS does in particular not require UHV conditions which are incompatible with the high vapour pressure of ice (see below).

(b) X-ray scattering allows a clear separation between long range order which gives rise to resolution-limited Bragg scattering and disorder inducing broad diffuse scattering signals. The analysis of the scattering distribution can be done within a straightforward kinematic theory relating the recorded scattering intensity to the atomic correlations by a simple Fourier transform.

(c) In the evanescent regime (i.e. within the regime of total external reflection) the depth of the probe

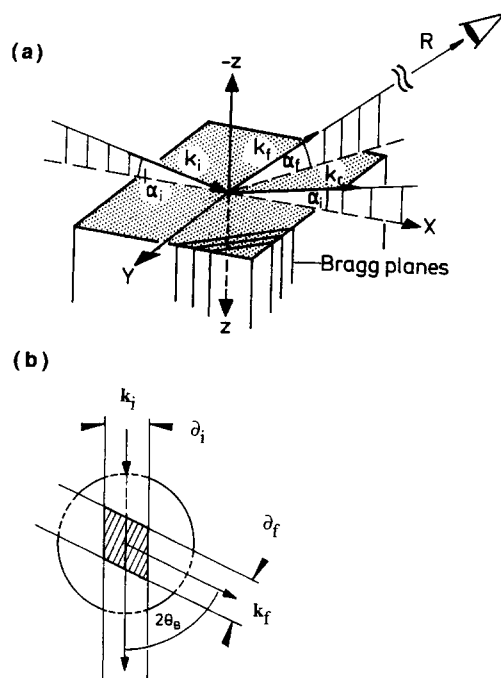


Fig. 2. Glancing angle scattering geometry (schematic): (a) $k_{i,f,r}$ denote the incident, diffracted and specularly reflected beam, respectively. (b) Top view showing the active surface area (hatched) as determined by the slits ∂_i and ∂_f .

can conveniently be tuned between several ångström (typically 50 Å) for shallowest angles and more than 10^4 Å for angles well above the critical angle.

The principle of GAXS is depicted in Fig. 2. The monochromatic, highly brilliant synchrotron-X-ray beam (k_i) hits the ice surface at a shallow angle α_i around the critical angle (α_c) for total external reflection and creates the specularly reflected beam (k_r) as well as the evanescent wave field (with complex wave vector denoted k'_z , see below) within a thin surface skin. Owing to the low average electron density of Ih ice, $\rho_e = 0.307 \text{ e}/\text{\AA}^3$, α_c is rather small:

$$\alpha_c(\text{ice})/\lambda = 1.66 \text{ mrad}/\text{\AA}, \quad (2)$$

thus, typical incidence angles in such experiments are $\alpha_i = \alpha_c/2 = 0.14^\circ$ for $\lambda = 1.5 \text{ \AA}$. Fig. 2b shows the top view and the “active surface area” defined by the in-plane slits $\partial_{i,f}$ for k_i and k_f . In the experiments described below we are mostly considering Bragg scattering from the evanescent X-ray wave excited from Bragg nodes $G_{hk,l}$ which lie in the surface (see Bragg planes in Fig. 2a). The associated Bragg intensity is observable at an in-plane Bragg angle $2\theta_B$ (Fig. 2b) and at a glancing exit angle α_f (for reviews of this scheme see Refs. [18,19]). Within the distorted wave Born approximation (DWBA) the scattering cross section equals [20]

$$\frac{d\sigma}{d\Omega} = |r_e T_i T_f^* F|^2 P S(\mathbf{Q}_{\parallel}, Q'_z), \quad (3)$$

where r_e is the classical electron radius, F the structure amplitude of the hexagonal Ih ice unit cell and P a polarization factor. $T_{i,f}$ is the transmission function of the interface associated with the incoming and diffracted beam which gives rise to the well-known intensity enhancements, whenever α_i or α_f are closest to α_c . The arbitrary kinematic scattering function $S(\mathbf{Q}_{\parallel}, Q'_z)$ depends on the in-plane scattering vector \mathbf{Q}_{\parallel} and on the refracted scattering vector component perpendicular to the surface,

$$Q'_z = k'_{iz} - k'_{fz}, \quad (4)$$

with

$$k'_{i,fz} = k \left(\alpha_{i,f}^2 - \alpha_c^2 + \frac{i\mu\lambda}{2\pi} \right)^{1/2}, \quad (5)$$

μ as the linear absorption coefficient and $k = 2\pi/\lambda$. In the case of Bragg scattering from an ideal crystal surface $S(\mathbf{Q}_{\parallel}, Q'_z)$ is given by [21,22]

$$S(\mathbf{Q}_{\parallel}, Q'_z) = \frac{1}{|1 - e^{iQ'_z d_z}|^2} \delta(\mathbf{Q}_{\parallel} - \mathbf{G}_{hk,l}), \quad (6)$$

with d_z being the lattice spacing perpendicular to the surface.

In the subsequent data analysis we have to include essentially three deviations from this ideal situation: the loss of lateral long range order (surface melting), surface roughening and thermal faceting.

By the appearance of a disordered surface sheet of thickness $L_d(T)$ which contributes no longer to the Bragg signal, but still to the refraction effects, $S(\mathbf{Q}_{\parallel}, Q'_z)$ suffers a damping described by the factor [21,22]

$$\Gamma_{L_d}(Q'_z, T) = e^{-2L_d(T)|\text{Im}(Q'_z)|}, \quad (7)$$

which is most pronounced for small values α_i and α_f . The quantity

$$\Lambda = |\text{Im } Q'_z|^{-1} \quad (8)$$

is called “scattering depth” and measures the effective escape depth of the diffracted X-rays in the evanescent regime. Fig. 3 shows Λ for various glancing angles (full lines). Typically Λ can be tuned in ice between 70 Å and 10^4 Å. Also shown in Fig. 3 is $q_z = \text{Re}(Q'_z)$ in the range of glancing angles (dashed lines): Since q_z is very close to 0, evanescent Bragg scattering is rather insensitive to surface roughness, however, a small damping in the Bragg

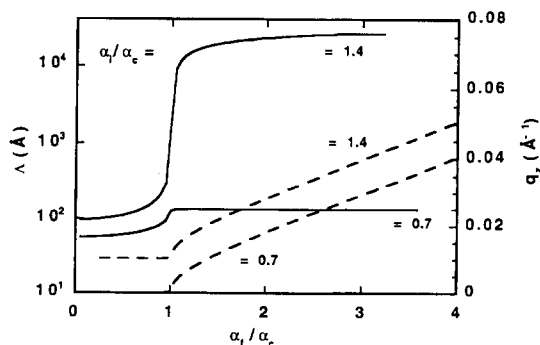


Fig. 3. Scattering depth Λ (full lines) and perpendicular momentum transfer q_z (dashed lines) in ice versus α_f/α_c for $\alpha_i/\alpha_c = 0.7$ and $\alpha_i/\alpha_c = 1.4$.

profile may be observed, when α_i and α_f are beyond α_c entailing $q_z \neq 0$. A rms roughness $\rho(T)$ (which includes static roughness as well as thermal vibrations in z -direction) then gives rise to a relatively small damping [18,23]

$$\Gamma_\rho^{(1)}(Q'_z, T) = e^{-2\rho^2(T)(q_z^2 - \Lambda^{-2})}. \quad (9)$$

Note that surface roughness also modifies the transmission functions $T_{i,f}$ in Eq. (3) by the factor

$$\Gamma_{\rho i,f}^{(2)} = e^{\rho^2(T)(k_{i,fz} - k'_{i,fz})/2}. \quad (10)$$

Thus, in the presence of roughness and lateral disorder, the evanescent Bragg scattering reads

$$\tilde{S}(Q_\parallel, Q'_z) = \Gamma_{L_d} \Gamma_\rho^{(1)} | \Gamma_{\rho i}^{(2)} \Gamma_{\rho f}^{(2)} |^2 S(Q_\parallel, Q'_z). \quad (11)$$

In Eq. (11) the influence of facets of various orientations is not included. This has recently been discussed in the context of the X-ray characterization of ice surfaces [17]: Consider Fig. 4a showing the surface of a facet which is tilted with respect to the average surface with surface normal n_s . Quite generally we describe the tilt by two angles γ_1 and γ_2 in the in-plane directions s_1 and s_2 , respectively, as e.g. $\langle 11.0 \rangle$ and $\langle 00.1 \rangle$ at the $\{11.0\}$ surface. Thus, for the $(\bar{h}h.0)$ Bragg node excited at glancing angles α_i and α_f (with respect to the average surface) the actual glancing angles associated with a facet tilted by γ_1 and γ_2 are shifted by (see Fig. 4a)

$$\Delta\alpha_{i,f} = \gamma_1 \cos \theta_{\bar{h}h.0} + \gamma_2 \sin \theta_{\bar{h}h.0}. \quad (12)$$

While a nonzero $\Delta\alpha_i$ modifies the overall Bragg intensity, the exit angle offset $\Delta\alpha_f$ displaces the α_f -position of the Bragg profile by $\Delta\alpha_f$. The latter can directly be observed in the experiment. In Fig. 4b we show a DWBA simulation of the effect of a tilted facet on the Bragg profile. Note already here the distinct intensity changes originating from the different tilt angles. They are mediated solely by T_i in Eq. (3). By measuring various inplane Bragg nodes associated with one facet, the exact tilt of the facet can be determined by triangulation.

4. Sample preparation and in situ sample chamber

Reliable glancing-angle X-ray experiments require the controlled preparation of flat, mirrorlike ice

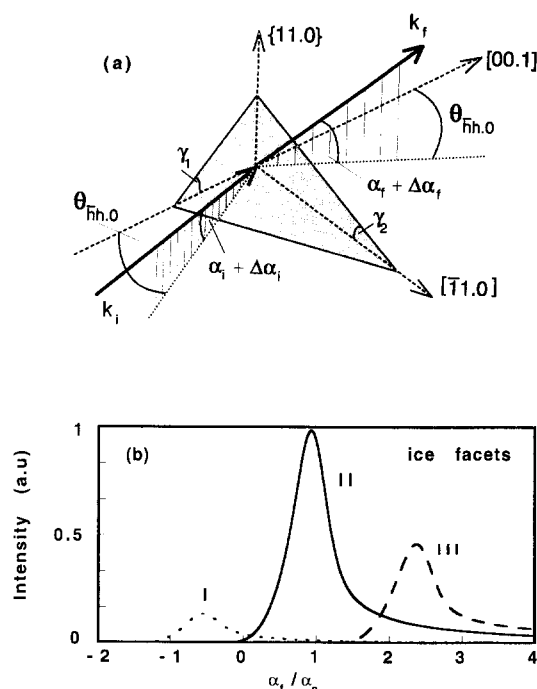


Fig. 4. Influence of facets on glancing angle Bragg profiles: (a) Scattering geometry (see text). (b) Numerical simulation of (00.2) reflection at the prism surface for various facet orientations: $\gamma_{1,2} < 0$ (I), $\gamma_{1,2} = 0$ (II), $\gamma_{1,2} > 0$ (III).

surfaces which have a high single-crystal quality. It is mandatory that this quality is preserved during the time period between preparation and the actual X-ray experiment and particularly throughout the entire X-ray experiment. In the following we describe a sample and surface preparation procedure which finally allowed us to obtain very reproducible results between various samples and during one experiment at one ice surface which lasted typically as long as one week.

Ice single crystals of cylindrical shape have been grown from “millipore” water (electrical conductivity $\sigma \leq 10^{-7} (\Omega \text{ cm})^{-1}$) by iterative zone melting. The concentration of organic impurities (as CO_2) in these high quality crystals is less than 10^{-9} , the dislocation density only around 10^3 cm^{-2} . More details on the bulk properties of ice are described in Ref. [24]. In order to avoid any mechanical damaging of the crystal (see Refs. [24,25]), a most gentle further preparation has been carried out in a walk-in cold room ($T \cong -15^\circ\text{C}$). By means of an electrically

heated wire a sample of typically 30 mm thickness and of a surface area of several cm² has slowly been “cut” out of the crystal and mounted on a goniometer head within a small, cooled capsule which is then transferred onto a two-circle X-ray diffractometer, where the required surface orientation is adjusted (with a typical error of 0.02°). The aligned goniometer-sample assembly is then moved to the surface preparation stage as depicted in Fig. 5a. It consists of an optical bench, where the oriented sample as well as a mirror-like glass plate are mounted along the optical axis. The glass temperature can be controlled between -20°C and $+15^{\circ}\text{C}$ by a Peltier element. By means of a translation stage the glass plate (heated to slightly above 0°C) is slowly pressed

against the sample (Fig. 5b), thereby the sample surface with the adjusted crystallographic orientation ($\{00.1\}$, $\{10.0\}$ or $\{11.0\}$ in our case) is created. It should be noted that a controlled continuous translation of the glass plate is required to keep the thickness of the (macroscopic) melt between the ice and the glass plate safely in the submillimeter range. This is necessary in order to avoid the risk of creating air inclusions within the liquid layer. Recrystallisation of the melt has to proceed very slowly ($\mu\text{m/s}$) starting from the ice-melt interface thereby assuring that a single crystal growth in a liquid epitaxy-like mode is achieved. This is achieved by keeping the temperature of the glass plate around -3°C (but not cooler than -4°C), while the ice temperature stays

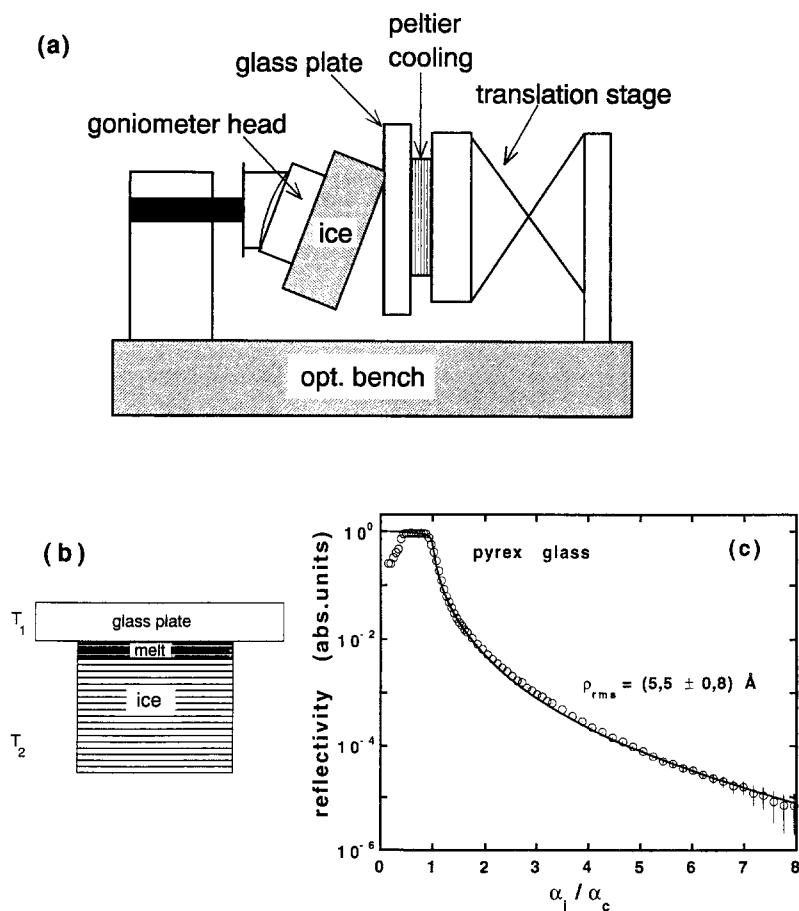


Fig. 5. Preparation of mirrorlike ice surfaces: (a) Optical bench with X-ray aligned ice on goniometer head and glass plate on a translational stage; (b) glass-ice assembly and temperatures $T_1 = 1^{\circ}\text{C}$, $T_2 = -6^{\circ}\text{C}$ associated with ice melting and $T_1 = -3^{\circ}\text{C}$, $T_2 = -6^{\circ}\text{C}$ associated with ice recrystallisation (see text); (c) X-ray reflectivity profile of pyrex glass with fit (full line) implying $\rho = (5.5 \pm 0.8) \text{ \AA}$.

at -6°C . After recrystallisation the whole ice-glass assembly is cooled to -15°C , then the ice crystal sticks very firmly to the plate (in fact any attempt to desintegrate the assembly would result in a cracking of the glass plate). It turns out that Pyrex glass is ideally apt for this part of the ice preparation: it can be prepared with a small waviness and a small micro-roughness and it is completely wetted by water. The surface roughness of the glass has been checked prior to the ice preparation by X-ray reflectometry (see Fig. 5c) giving typical values of 5–7 Å for the rms roughness. One of the main advantages of this surface preparation procedure is that such “glass-sealed” ice surfaces can be kept in a refrigerator ($T \cong -12^{\circ}\text{C}$) for several weeks, while free surfaces would deteriorate rather quickly because of extensive thermal etching.

Shortly before the X-ray investigations the sample is again transferred into a walk-in cold room closest to the experimental station at the Synchrotron radiation laboratory (here at HASYLab), where the glass plate is carefully tapped off at -6°C . The ice crystal with its mirrorlike surface is immediately mounted into a special insitu X-ray chamber which allows us to perform temperature-dependent X-ray scattering experiments for several days without loosing the surface quality. One challenge is the accurate control of the temperature and the vapour pressure of the gas phase. The experimental difficulties which one encounters here become clear when one recalls that any oversaturation inevitably leads to an almost immediate dendrite growth at the surface, while, on the other hand, undersaturation gives rise to severe thermal etching. Note that the sublimation rate is

$$\dot{S} = \alpha_s \frac{V_{\text{mol}} \Delta p}{(2\pi MRT)^{1/2}}, \quad (13)$$

with $\alpha_s = 0.14$ [26] and $V_{\text{mol}}, M, R, \Delta p$ the molar volume, the molar mass, the gas constant and the deviation from the saturation vapour pressure, respectively. Thus, at e.g. $T = -10^{\circ}\text{C}$ the exposure of the ice surface to a 90% saturated vapour still leads to a strong sublimation rate of $\dot{S} = 4.0 \mu\text{m/s}$, i.e. to an immediate macroscopic damage of the surface. The sample chamber described below allows the precise adjustment and stabilization of a relative undersaturation of $\Delta p/p \cong 2.5 \times 10^{-4}$ giving rise

to a controlled tiny sublimation rate of 10 Å/s at $T = -10^{\circ}\text{C}$ which does not lead, as it turns out (see Section 5), to noticeable disturbances in the thermodynamic surface phenomena.

The in-situ sample chamber is shown schematically in Fig. 6. The key component is a small capsule which contains the sample and, approximately 10 mm over its high quality surface, a second ice sample grown on a Cu plate whose temperature is controlled independently and kept typically 0.5°C below the actual sample temperature. In this way the ice reservoir at the Cu plate acts as a vapour source and a micro-getter pump for organic impurities and maintains a safely small sublimation rate at the single crystal surface. Temperature, pressure and humidity of the gas phase are continuously measured. The temperature of the sample and of the vapour source are controlled by Peltier elements, while the general temperature level of the entire chamber is maintained by a cooling liquid. A second vacuum chamber around the capsule provides thermal isolation. 360° Kapton windows allow access of the X-ray beam to the surface under investigation.

After the mounting of the ice crystal inside the capsule and after its thermal stabilization the chamber is transferred on the heavy-load X-ray diffractometer of the synchrotron radiation station, where the surface quality is analyzed by specular reflection and glancing-angle Bragg scattering. Fig. 7 shows by

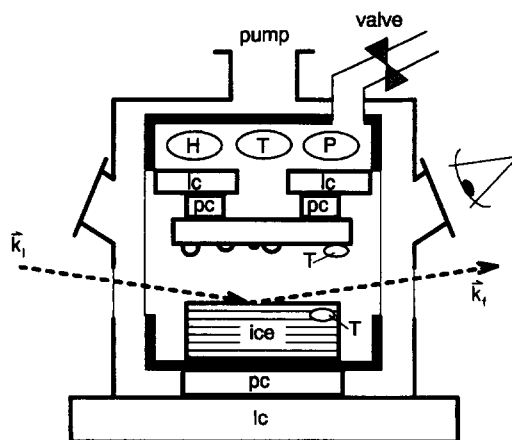


Fig. 6. In-situ X-ray chamber for ice experiments: lc = liquid cooling, pc = peltier cooling, T = temperature sensor, H = humidity sensor, p = pressure sensor, $k_{i,f}$ = wave vectors of the incoming and diffracted beam.

way of example typical results for the specular beam (Fig. 7a), the in-plane rocking width of the (00.2) reflection (Fig. 7b) and the out-of-plane profile (“rod profile”) of the ($\bar{3}$ 3.0) reflection (Fig. 7c) as observed at a {11.0} surface at $T = -15^\circ\text{C}$ after a 5 h sublimation cleaning of the surface. The width of the specular intensity is around 0.63 mrad as imposed by the waviness of the Pyrex glass. The inplane mosaicity of the surface sensitive (00.2) reflection is found to be as small as 0.02° (resolution limited) revealing a high quality single crystal surface. The least-squares fit of the out-of-plane profile within the DWBA

approximation (dashed line in Fig. 7c) confirms the excellent single crystal quality of the surface: We find a rms roughness of $\rho_{sv} = 10 \pm 2 \text{ \AA}$ (henceforth the subscript sv refers to the solid-vapor interface) and $L_d = 0$, i.e. no damaged layers at the surface (see Eq. (7)). Similar results have been found for all other surfaces. We note in particular that all surface sensitive Bragg signals showed at all temperatures resolution-limited in-plane widths. It is also worthwhile to mention that during the X-ray measurements the sample sublimates at a speed of $3.5 \mu\text{m/h}$, causing the surface to move out of the collimated

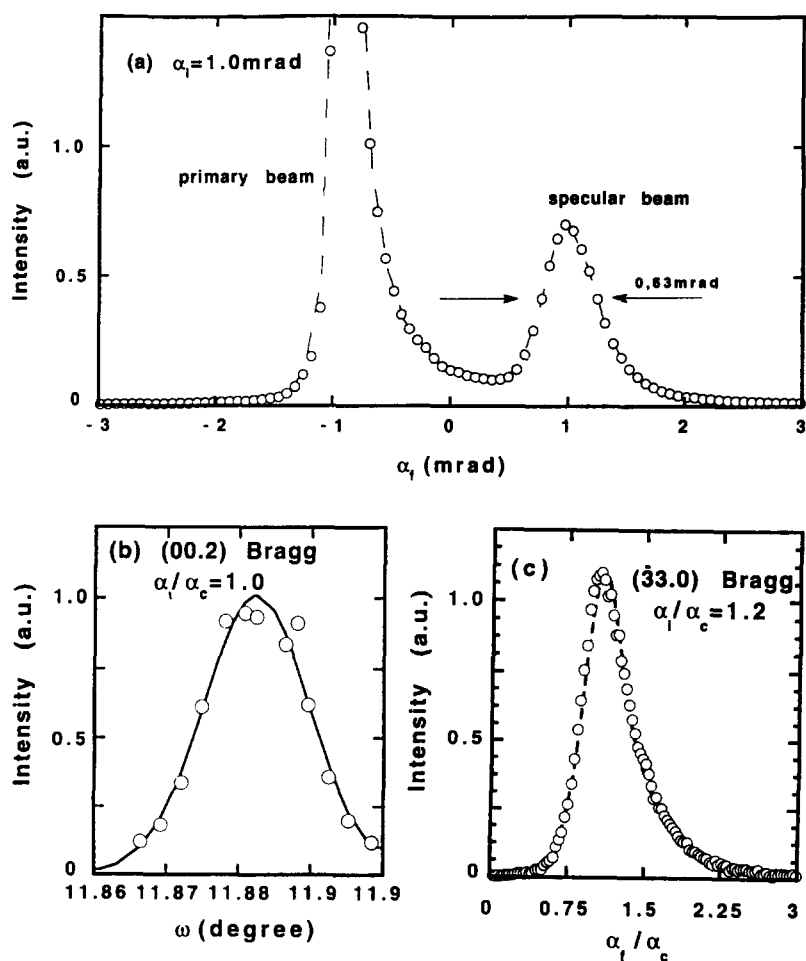


Fig. 7. Ice surface characterization with X-rays (here {11.0} surface): (a) specularly reflected beam for $\alpha_i = 1 \text{ mrad}$ (the left peak is due to the unblocked part of the primary beam). (b) in-plane rocking width (0.02°) of the (00.2) reflection (resolution-limited). (c) out-of-plane (α_i -) profile of ($\bar{3}$ 3.0) reflection taken from $\alpha_i / \alpha_c = 1.2 \alpha_c$. The dashed line is a theoretical fit with $L_d = 0$ and $\rho_{sv} = (10 \pm 2) \text{ \AA}$.

X-ray beam. This has to be carefully balanced by translating the sample chamber with the opposite velocity throughout the entire experiment.

5. Experimental results

The X-ray scattering studies have been carried out during several experimental runs at the Wiggler beam lines W1 and BW6 of HASYLab which are dedicated to surface work. Relevant experimental parameters, the various investigated ice surfaces and various Bragg profiles are summarized in Table 1. Bragg pairs like (10.0)–($\bar{1}$ 0.0) in Table 1 have usually been measured at low temperatures in order to determine independently the surface miscut $\Delta\phi$ from the ideal $hk.l$ orientation which affects both the Bragg intensity and the Bragg profile quite significantly in the evanescent regime [18].

All experimental data of these ice studies exploit the evanescent decay of X-ray field associated with total external reflection and the scattering depth effects shown in Fig. 3. The observed Bragg profiles have been analyzed within a DWBA formalism allowing for several thermally activated surface disordering mechanisms (see Section 2). In order to increase the reliability of the obtained parameters one common fit including several incidence angles has always been performed. As a direct check for the applicability of the semikinematic scattering theory to the high-quality ice surfaces we compared some low temperature integrated intensities of evanescent Bragg reflections with the expected semikinematic intensity which is [18]

$$I_{\text{int}}(\alpha_i, R) \cong \frac{I_0 r_e P \lambda^2 \alpha_i}{A_s \dot{\phi} \sin^2 2\theta} |T_i|^2 |F_{hk.l}|^2 \partial_i \partial_f \int_0^R d\alpha_f \times |T_f|^2 S_{hk.l}(\alpha_i, \alpha_f) \quad (14)$$

for small values of α_i and α_f . In Eq. (14) $\dot{\phi}$ is the angular scan velocity (sample rotation around surface normal), A_s the in-plane area of the unit cell and $S_{hk.l}(\alpha_i, \alpha_f)$ the Bragg scattering function associated with the glancing angles $\alpha_{i,f}$ including all microscopic deviations from the ideal surface (see Eq. (11)). The integral in Eq. (14) corresponds to the α_f -range from 0 to R as provided by the position sensitive X-ray detector. A typical example is the evanescent (10.0) reflection associated with the basal surface which has been measured at the BW6 station for $\alpha_i = 6$ mrad with the instrumental parameters $I_0 = 1.5 \times 10^{10}$ photons/mm²s (monochromatic photon flux at the sample position), $\partial_{i,f} = 2$ mm, $P = 0.15 + 0.85 \cos^2 2\theta$ (note that BW6 has a horizontal scattering plane), and a rocking speed $\dot{\phi} = 1.75$ μ rad/s, thereby accumulating 89400 counts in the detector. Using Eq. (14) we calculate $\cong 81500$ counts, thus, we conclude that the applied semikinematic scattering theory reproduces the observed evanescent ice Bragg reflection *on an absolute scale* to within an error of approximately 10%.

5.1. {00.1} surfaces

The experiments at the {00.1} surfaces (“basal planes”) have been performed between $T = -15^\circ\text{C}$ and the melting point. Fig. 8a,b shows some typical α_f -profiles of the (10.0) Bragg intensities as observed upon heating for two different angles of incidence. The most prominent effect is the strong intensity decay which should be compared with the expected thermal Debye–Waller factor damping: between -10°C and -0.5°C the bulk rms thermal amplitude shows an anharmonic increase by 17% [27,28] causing only a mild decrease of the low- Q (10.0) Bragg intensity by 4%, while at the surface the (10.0) Bragg profile has decayed by a factor of

Table 1
X-ray parameters of synchrotron radiation stations and ice reflections

| Exp. station (HASYLAB) | W1 | BW6 |
|--|--|--|
| X-ray source | 32-pole wiggler | 28-pole wiggler |
| Scattering plane | Vertical | Horizontal |
| Used wavelength | 1.735 Å | 1.520 Å |
| Slits: ∂_i, ∂_f (mm) | 2.0, 2.0 | 2.0, 2.0 |
| Resolution (mrad) $\delta\alpha_i, \delta\alpha_f, \delta\omega_{\parallel}$ | 0.5, 0.1, 0.2 | 0.3, 0.1, 0.1 |
| Flux at sample position (photons/mm ² s) | 1.4×10^{11} | 1.6×10^{10} |
| {Surface}: (Bragg) measured | {10.0}: (0.02, (0.0.2) (00.6), (00.6) | {00.1}: (10.0), ($\bar{1}$ 0.0) {11.0}: (33.0), (00.2) |

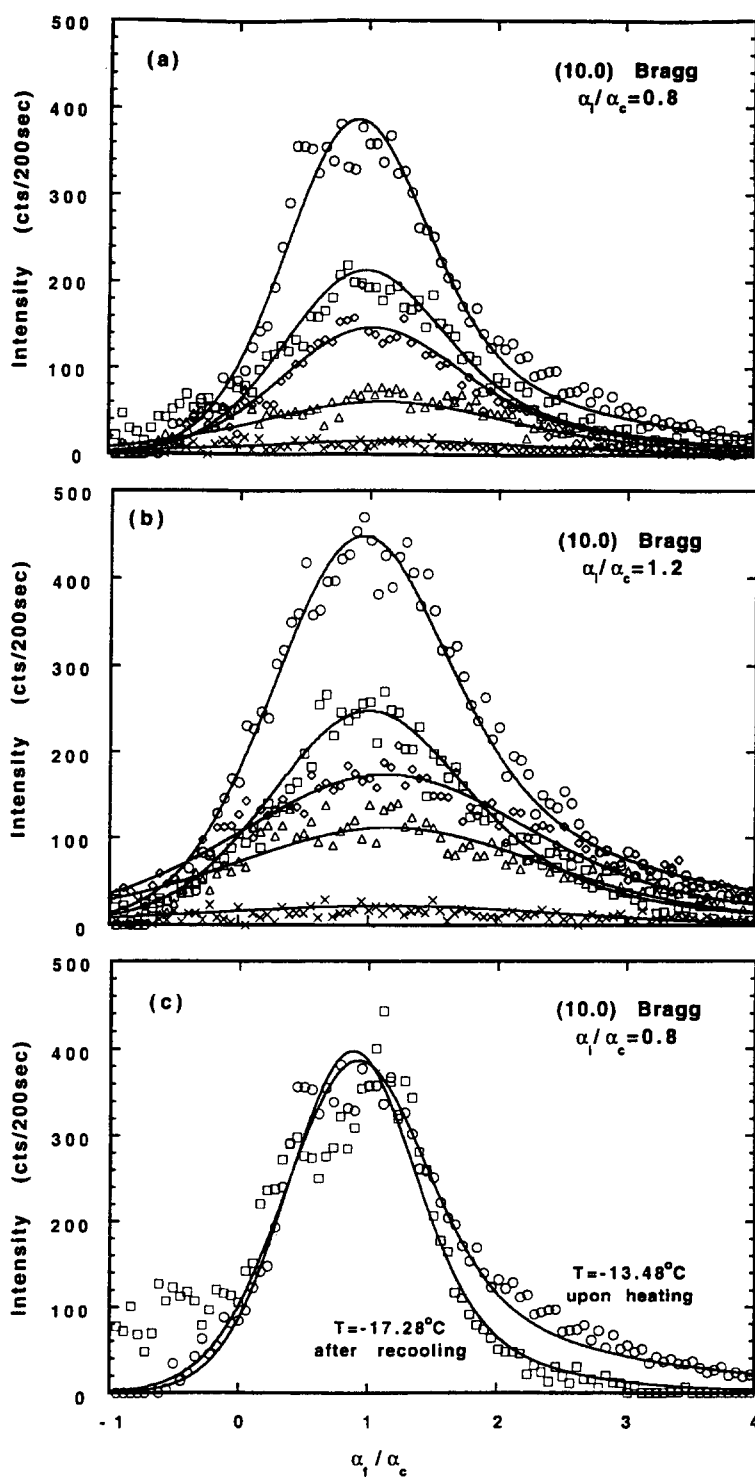


Fig. 8. Temperature dependence of the (10.0) α_f -profile as observed at {00.1} surfaces together with theoretical fits (full lines) for $T = -13.48^\circ\text{C}$ (\circ), $T = -9.28^\circ\text{C}$ (\square), $T = -6.73^\circ\text{C}$ (\diamond), $T = -4.46^\circ\text{C}$ (\triangle) and $T = -1.15^\circ\text{C}$ (\times) and for (a) $\alpha_i/\alpha_c = 0.8$ and (b) $\alpha_i/\alpha_c = 2.4$. (c) Comparison of the α_f -profiles recorded at $\alpha_i/\alpha_c = 0.8$ upon heating ($T = -13.48^\circ\text{C}$ (\circ)) and after recooling from $T = -1.15^\circ\text{C}$ ($T = -17.28^\circ\text{C}$ (\square)). The nonzero scattering at $\alpha_f < 0$ upon recooling (\blacksquare) originate from emerging macrosteps (see also Fig. 10 and main text).

≈ 20 within this temperature range. This indicates, without applying a detailed quantitative analysis, a strong thermal disorder which emerges at the $\{00.1\}$ surface. It should be noted that the low-temperature Bragg profiles are perfectly recovered upon cooling; only for larger values of α_f some irreversible intensity losses are detected (Fig. 8c) and will be discussed later. The full lines in Fig. 8 are the best fits within the DWBA, essentially based on Eq. (11). The underlying model includes a temperature-dependent disordered layer thickness L_d , thermal roughness ρ_{sv} at the solid–vapour or solid–quasiliquid interface (denoted ρ_{sl} as a quasiliquid emerges) and

changes in the effective waviness of the solid–quasiliquid interface. The latter is measured in the experiment as a smearing $\delta\alpha$ of both glancing angles and is thus accounted in the data analysis by integrating $d\sigma/d\Omega$ (Eq. (3)) properly over $\delta\alpha$. As a result of this analysis we find that the strong decrease in the Bragg intensity and the change in the α_f -profile is best reproduced by introducing a disordered surface sheet of thickness L_d . The temperature dependence of L_d is shown in Fig. 9a demonstrating that the basal plane remains well-ordered up to $T \cong -13^\circ\text{C}$. At higher temperatures a disordered surface layer (denoted “quasiliquid” in the following) appears

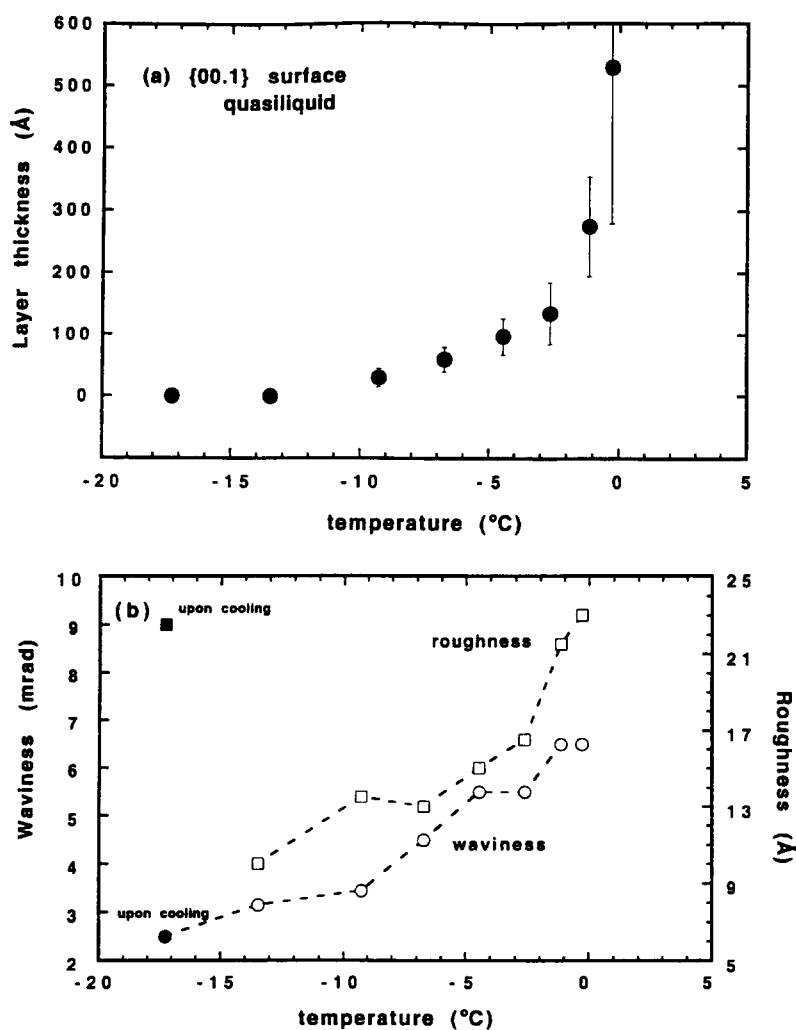


Fig. 9. Fit parameters describing thermal disorder at the $\{00.1\}$ surface: (a) thickness of quasiliquid (L_d) versus T ; (b) roughness ρ_{sv} , ρ_{sl} (\square) and waviness (\circ) versus T (the full symbols have been measured upon recooling).

growing to thickness of approximately 500 Å at $T = -0.3^\circ\text{C}$. Most interestingly the appearance of a quasiliquid surface layer is accompanied by two other surface effects: a thermal increase of the mesoscopic waviness and of the roughness of the solid-quasiliquid interface (Fig. 9b). It turns out that the appearance of the quasiliquid and of the waviness are completely reversible with temperature (see full symbol (●) in Fig. 9b), but the roughness parameter ρ_{sv} is not, as can directly be seen from Fig. 8c which shows that upon the intensity profile remains low upon cooling at larger values of α_f (see also full symbol (■) in Fig. 9b). Apparently, the large interfacial roughness at the diffuse solid-quasiliquid interface is frozen in when the quasiliquid has disappeared. It is unclear right now, whether this is a diffusion-limited irreversibility.

Fig. 10 shows the (10.0) Bragg profile along a more extended α_f scale as observed some hours after the start of the experiment: in addition to the surface Bragg profile for $\alpha_f \geq 0$ (which disclosed the surface disordering phenomena discussed before) a strong Bragg scattering has appeared at $\alpha_f = 2\Delta\phi\sin\theta - \alpha_i$, i.e. below the sample surface horizon “ $\alpha_f = 0$ ” ($\Delta\phi$ is the surface miscut angle). This additional Bragg scattering signal results from

macrosteps which give rise to an unrefracted Bragg scattering process in transmission geometry. The formation of macrosteps is induced in our experiments by the steady sublimation at the surface. The same phenomena have been observed in scanning electron microscopy studies which have also been performed under the condition of undersaturation and in recent Monte Carlo simulations [30].

5.2. {10.0} surfaces

As a typical example of our findings at prism surfaces we discuss the (00.2) reflection: from the intensity analysis of the (00.2)–(00.2̄) pair (as measured at low temperatures) we deduce a surface miscut of $\Delta\phi = -6.7 \pm 0.2$ mrad in the $\langle 00.1 \rangle$ direction. Fig. 11a shows the associated (00.2) reflection profiles as observed at $\alpha_i = 0.7\alpha_c$ for several temperatures between -20.22°C and -1.05°C . We observe changes in the position, intensity and shape of the α_f -profiles as a function of temperature. The detailed analysis of these Bragg scattering profiles within the DWBA (full lines in Fig. 11a), however, gives a consistent picture of the surface phenomena: The distinct change of the α_f -position shows that the prism surface decomposes into facets

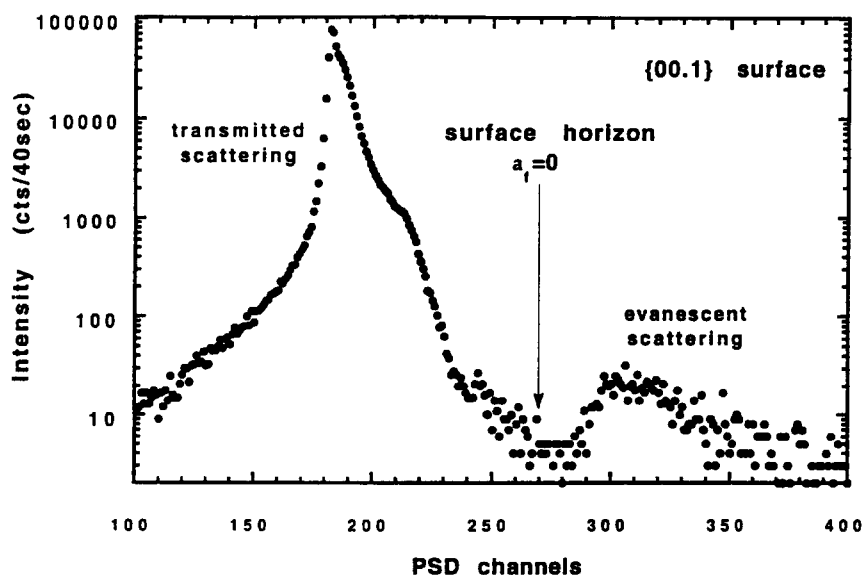


Fig. 10. Extended {10.0} α_f -profile at the {00.1} surface showing the surface-related Bragg reflection (for $\alpha_f > 0$) and a (nonrefracted) transmitted Bragg contribution below the surface horizon (for $\alpha_f < 0$).

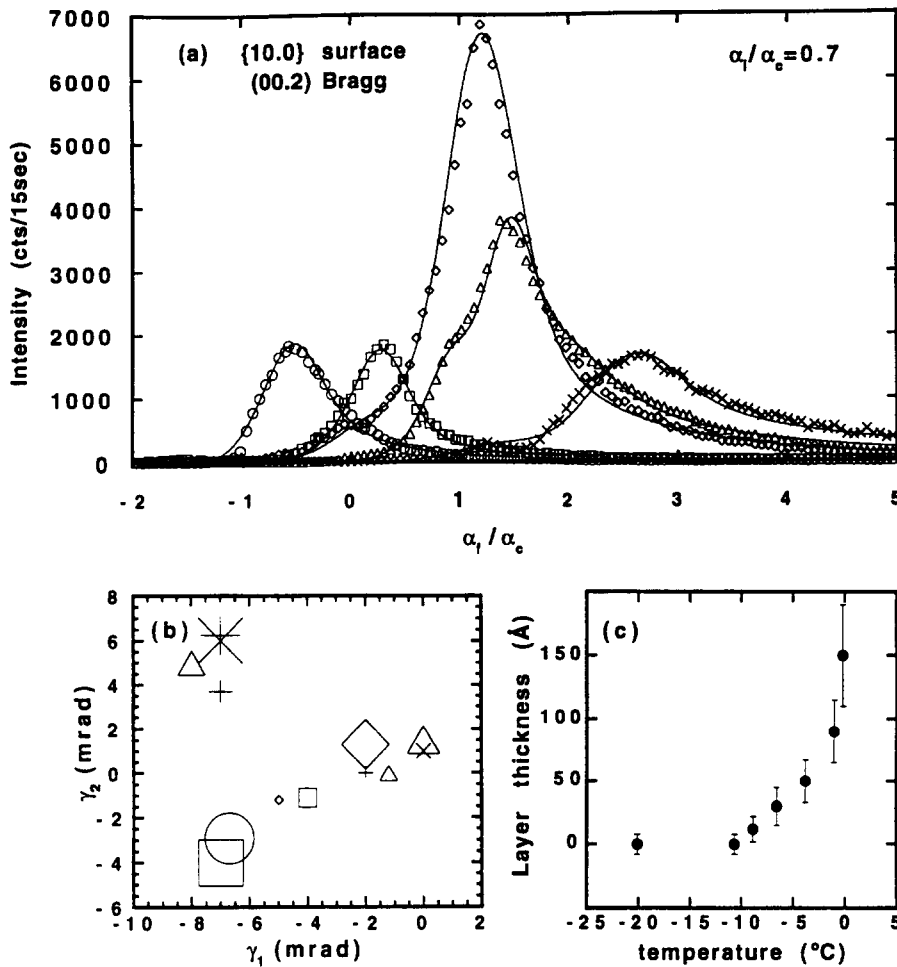


Fig. 11. Experimental results from the {10.0} surface: (a) Temperature dependence of the (00.2) α_r -profile for $\alpha_i/\alpha_c = 0.7$ and for $T = -20.22^\circ\text{C}$ (\circ), $T = -8.87^\circ\text{C}$ (\square), $T = -6.60^\circ\text{C}$ (\diamond), $T = -3.81^\circ\text{C}$ (\triangle), $T = -1.05^\circ\text{C}$ (\times). The full lines are best fits within the DWBA. (b) Observed surface horizons described by the tilt angles γ_1 and γ_2 with respect to the average surface (with miscut angle $\Delta\phi = 6.7$ mrad) for various temperatures. The symbols refer to the temperatures explained in Fig. 11a, the symbol sizes reflect the visible facet areas. (c) Thickness of quasiliquid surface sheet versus temperature.

depending on the temperature: At $T = -20.22^\circ\text{C}$ the fitting reveals that there is only one facet present being tilted with respect to the average (vicinal {10.0}) surface by $\gamma_1 = 6.7 \pm 0.6$ mrad in the $\langle 00.1 \rangle$ direction and by $\gamma_2 = -2.9 \pm 0.3$ mrad in the $\langle 11.0 \rangle$ direction. The observed relation $\gamma_1 + \Delta\phi = 0$, means that the observed facets are the ideal {10.0} surface planes. The least-squares fit of the associated α_r -profile (full line in Fig. 11a) gives $L_d = 0 \pm 5$ Å and $\rho_{sv} = 12 \pm 3$ Å implying that the facets are dry and well-ordered. From absolute measurement of the evanescent Bragg intensity the total surface area of

these prism facets can be deduced: with $I_0 = 1.5 \times 10^{11}$ photon/mm²s (W1 station) and a rocking speed of $\dot{\phi} = 11.65$ $\mu\text{rad/s}$ we observe 57200 counts in the position sensitive detector. Since, according to Eq. (14) we expect 59500 counts, the surface is apparently decomposed almost completely into ideal prism facets ("saw tooth"-like morphology). Upon heating the facet structure changes as monitored by the moving horizons of the various Bragg profiles. Fig. 11b shows the result of a detailed analysis of the tilt angles and the effective area of the emerging new horizons when the surface is heated up to -0.21°C .

When the ice temperature is increased to -6.6°C , the prism horizons are gradually replaced by a horizon distribution around the mean surface ($\gamma_1 = \gamma_2 = 0$). As will be discussed below in detail this change in the optical horizon is accompanied by strong surface melting. In fact there is a good argument that the new optical horizon which slowly emerges at $\gamma_1 \approx \gamma_2 \approx 0$ is mediated by surface melting. Therefore, we first discuss the thermal behaviour of the quasiliquid surface layer and come back to the facets later.

Due to the changing optical horizon which strongly affects the evanescent Bragg intensity the emergence of a quasiliquid surface sheet cannot merely be seen from Fig. 11a. Note in particular that the strong Bragg intensity associated with $T = -6.6^\circ\text{C}$ is purely mediated by the surface enhancement of the X-ray transmission function at $\alpha_f = \alpha_c$ (see Section 3). However, the detailed analysis of the temperature evolution of the α_f -profiles (full lines) reveals a strong damping of $S(Q_{\parallel}, Q_z)$ and gives by this a clear evidence for surface melting at the prism facets: according to Fig. 11c, which shows the fit parameter L_d versus T , a disordered surface sheet starts to emerge around -12.5°C and grows to thickness of 150 \AA at -1.05°C . In contrast to our findings for the basal surface the microscopic roughness and the surface waviness remain almost constant at $\rho_{sl} \approx 10 \pm 3 \text{ \AA}$ and $\delta\alpha = 1.5 \pm 0.3 \text{ mrad}$, respectively.

With this experimental result we return to the discussion of Fig. 11b and the appearance of a new surface horizon upon heating to $T = -6.6^\circ\text{C}$. We note that the average thickness of the quasiliquid layer at this temperature is $L_d \approx 60 \text{ \AA}$. The step-height between two neighbouring prism facets, on the other hand, is $h_{\Delta\phi} = \zeta\Delta\phi$ (ζ being the linear dimension of the facet), thus, with $\Delta\phi = 6.7 \text{ mrad}$ and $\zeta \approx 2000 \text{ \AA}$ we get $h_{\Delta\phi} \approx 20 \text{ \AA}$. This implies that the thickness of the quasiliquid associated with $T = -6.6^\circ\text{C}$ already exceeds the step height between neighbouring prism facets ($L_d \geq h_{\Delta\phi}$) and creates by this a new optical surface close to the vicinally cut surface. Near the melting point a slight rounding of the surface could be detected optically. In this regime the actual surface horizon depends upon the location of the active surface area at the ice surface (see Fig. 2b). It turns out that the seemingly new surface

horizon for $T = -1.03^\circ\text{C}$ and -0.21°C in Fig. 11b is induced by a slightly off-centered active surface area and is thus not relevant. It should be noted that the thickness of the observed surface disorder is reversible with temperature. We also recovered the low-temperature prism facets upon cooling.

5.3. $\{11.0\}$ surfaces

The results obtained from $\{11.0\}$ surfaces are qualitatively similar to those for the $\{10.0\}$ surface. Fig. 12a,b shows the (00.2) and ($\bar{3}3.0$) Bragg profiles as measured at a freshly prepared $\{11.0\}$ surface between $T = -11.48^\circ\text{C}$ and $T = -0.21^\circ\text{C}$ for (a) $\alpha_i/\alpha_c = 1.0$ and (b) $\alpha_i/\alpha_c = 1.2$. Again we find a distinct temperature dependence of the Bragg profiles in position, intensity and shape which originates from a faceting and disordering of the surface. The full lines are least-squares fits which describe the thermal changes of all evanescent Bragg profiles with one common set of parameters very well. Figs. 12c and 12e show the rms thermal amplitude $\langle u^2 \rangle^{1/2}$ parallel to the $\{11.0\}$ surface (as averaged over the escape depth of the evanescent scattering process) and the thickness of the disordered surface layer (L_d). The first quantity is accessible via the evanescent ($\bar{3}3.0$) reflection which has a large parallel momentum transfer, $G_{\bar{3}3.0} = 4.81 \text{ \AA}^{-1}$: Up to $T = -4.21^\circ\text{C}$, $\langle u^2 \rangle^{1/2}$ is consistent with a harmonic behaviour, i.e., $\langle u^2 \rangle^{1/2} \sim T$. The measured value $\langle u^2 \rangle^{1/2} \approx 0.21 \text{ \AA}$ around $T = -10^\circ\text{C}$ is roughly the bulk value. At higher temperatures, however, strong anharmonic contributions lead to a significant damping of the ($\bar{3}3.0$) reflection: close to the bulk melting point, the rms amplitude reaches an enhanced value of 0.32 \AA . Since qualitatively similar results have been observed in bulk ice between -10°C and -0.5°C [27], it is not clear at the moment, whether our findings require the introduction of additional surface-induced anharmonicities.

Owing to the small miscut of this surface with respect to the $\{11.0\}$ direction the decomposition into ideal $\{11.0\}$ facets at low temperatures is less visible. The intensity and line shape analysis of the (00.2) and ($\bar{3}3.0$) α_f -profiles can, however, unambiguously be described by assuming essentially two surface horizons with varying surface area as a function of temperature (Fig. 12d): at low temperatures only one

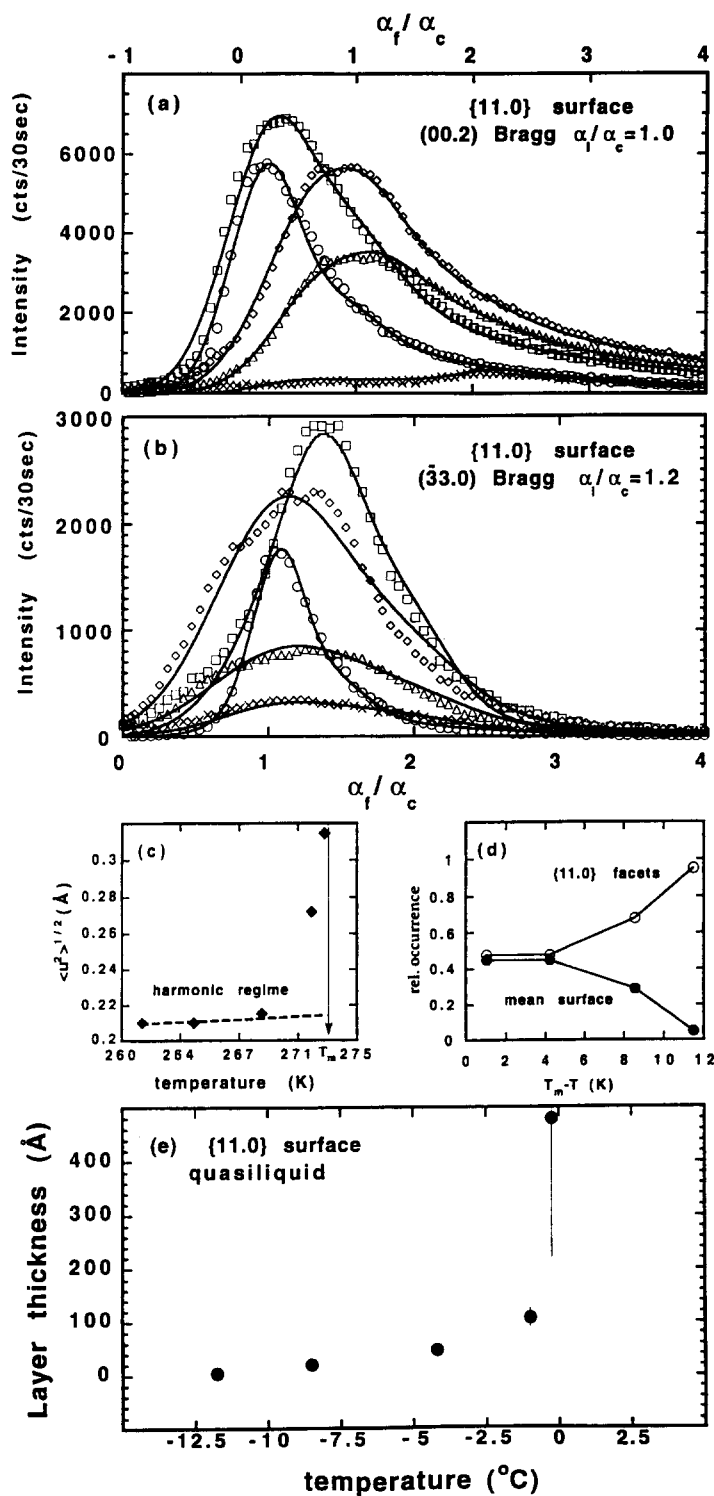


Fig. 12. X-ray observations at the {11.0} surface: (a) (00.2) α_f -profiles measured at $\alpha_f/\alpha_c = 1.0$ and (b) ($\bar{3}3.0$) α_f -profiles measured at $\alpha_f/\alpha_c = 1.2$ for $T = -11.48^\circ\text{C}$ (\circ), $T = -8.56^\circ\text{C}$ (\square), $T = -4.21^\circ\text{C}$ (\diamond), $T = -1.03^\circ\text{C}$ (\triangle), and $T = -0.21^\circ\text{C}$ (\times). (c) Near surface $\langle u^2 \rangle^{1/2}$ versus temperature. (d) Temperature dependence of the effective surface area of the ideal {11.0} facets ($\gamma_1 = -1.6$ mrad, $\gamma_2 = -1.0$ mrad) (open symbol) and of the mean surface ($\gamma_1 \approx \gamma_2 \approx 0$) (full symbol). (e) Thickness of quasiliquid surface sheet versus temperature.

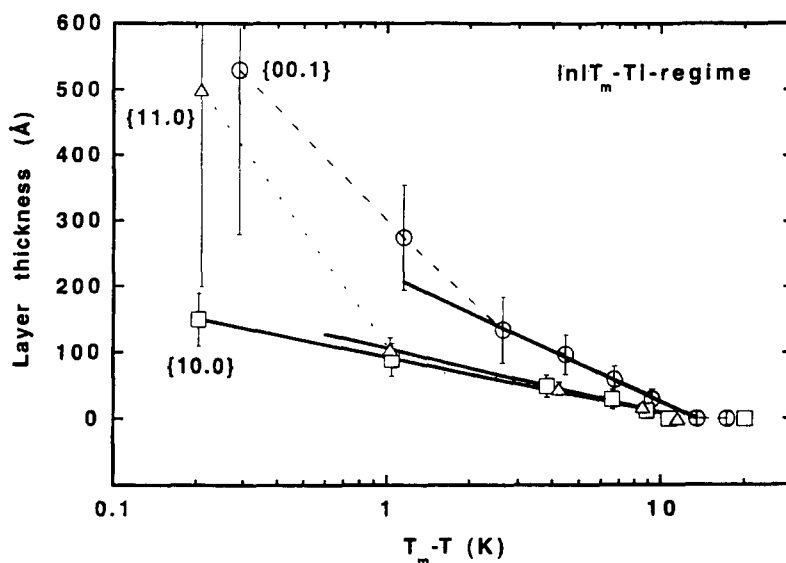


Fig. 13. Measured values L_d associated with the {00.1} surface versus $\ln |T_m - T|$. The straight lines define the range dominated by exponentially decaying interactions implying the results summarized in Eq. (18).

facet (\circ) with $\gamma_1 = -1.6$ mrad and $\gamma_2 = -1.0$ mrad (associated with the ideal {11.0} facets) is present. Upon heating the emerging quasiliquid slowly creates a new surface horizon at $\gamma_1 \approx \gamma_2 \approx 0$ (\bullet) (associated with the original miscut orientation).

6. Discussion of the results

Our X-ray results give strong evidence that surface melting occurs at all three high symmetry surface of hexagonal ice, setting in at $T_s \approx -13.5^\circ\text{C}$ and $\approx -12.4^\circ\text{C}$ on basal and nonbasal surfaces, respectively. We observed that basal surfaces don't show any significant faceting, while the (slightly vicinally prepared) nonbasal surface decompose into the ideal {10.0} and {11.0} facets, respectively. The emerging quasiliquid surface layer steadily replaces the horizon associated with the ideal facets by a new surface horizon close to the average surface. In what follows we will discuss our results quantitatively in the light of the previous experimental evidence of surface melting of ice and in view of general surface melting rules.

Quite generally surface melting should occur, when the interfacial energies γ_{sv} , γ_{sl} and γ_{lv} associated with the solid-vapour, solid-quasiliquid and

quasiliquid-vapour interface, respectively, fulfil the inequality $\Delta\gamma \equiv \gamma_{sv} - (\gamma_{sl} + \gamma_{lv}) \geq 0$. In the case of H_2O only γ_{lv} is exactly known, $\gamma_{lv} = 76 \text{ mJ/m}^2$, while γ_{sv} and γ_{sl} have to be deduced from the number B_H of cut H-bonds per surface area A across the interface, i.e.

$$\gamma_{sv} = \frac{1}{2} \left(\frac{B_H}{A} \right)_{hk.l}, \quad (15)$$

$$\gamma_{sl} \approx \gamma_{sv} \frac{\lambda_m}{\lambda_s},$$

whereby $\lambda_m/\lambda_s = 0.12$ is the ratio between the latent heat of melting and the heat of sublimation. We find $\gamma_{sv} = 120 \text{ mJ/m}^2$ and $= 128 \text{ mJ/m}^2$ for basal and prism surfaces, respectively, thus, (ignoring here the $hk.l$ -dependence of γ_{sv}) $\gamma_{sl} \approx 15 \text{ mJ/m}^2$ and $\Delta\gamma \approx 35 \text{ mJ/m}^2 (\geq 0)$. This tells us firstly that surface melting should occur at all the investigated surfaces and secondly that the quasiliquid-vapour interface should be relatively sharp, while the solid-quasiliquid interface (governed by the small interfacial energy γ_{sl}) should be rather diffuse. These conclusions are apparently confirmed by our experiments. A diffuse solid-quasiliquid is, however, only found at the basal surface, where a strong thermal waviness and

roughness of the solid–quasiliquid interface is found (Fig. 9a,b), while the investigated nonbasal surfaces exhibit within our sensitivity and within the experimental temperature regime a flat solid–quasiliquid interface.

Since melting is a first-order phase transition, the microscopic details of surface melting are expected to depend strongly on details of the system, as on the underlying interactions and on the structural properties of the surface under consideration. However, from quite general reasoning, one can conclude that around the onset of surface melting the layer thickness should grow as [31]

$$L_d = A_d \ln |T_s / (T_m - T)|. \quad (16)$$

This growth scenario has been confirmed experimentally at {110} surfaces of fcc metals, like Pb and Al [32]. It turns out that the growth amplitude A_d is given by the leading length scale ξ_{qll} in the problem [31]: When the solid–quasiliquid interface is flat (nonrough), ξ_{qll} is determined either by the correlation length of the bulk liquid, i.e. $\xi_{qll} = \xi_b$, or by a new substrate-dominated correlation length. When the solid–quasiliquid interface is strongly fluctuating (rough), another length scale $\xi_{qll} = (kT/2\pi\gamma_{sl})^{1/2}$ governs the scenario (for additional comments see footnote [33]). The onset temperature for surface melting which appears in Eq. (16) is related to $\Delta\gamma$ by [31]

$$T_s = T_m \frac{\Delta\gamma}{A_d \lambda_m}. \quad (17)$$

In order to test whether the measured values of L_d on ice surfaces obey this initial growth law, we plot L_d versus $\ln |1/(T_m - T)|$ (Fig. 13). The full lines are the best linear fits to the data showing that a logarithmically growing quasiliquid layer can be detected up to $T = -2.5^\circ\text{C}$ at basal surfaces, up to $T = -1.0^\circ\text{C}$ at {11.0} surfaces and up to the highest measured temperature, $T = -0.2^\circ\text{C}$, at {10.0} surfaces. Apparently, the window for occurrence of the $\ln |1/(T_m - T)|$ -law is not given by a typical upper temperature, but by an upper critical film thickness, $L^* \cong 150 \text{ \AA}$. As the film thickness exceeds L^* a much stronger surface melting sets in, as clearly observed at the basal surface. Interestingly, L^* appears close to another characteristic length in ice

being related to a crossover between the UV dielectric constants of water and ice at $\omega = 2 \times 10^{16} \text{ s}^{-1}$ [34]. The associated length $L_{\text{ret}} = c_0/\omega = 150 \text{ \AA}$ (c_0 being the speed of light) is essentially equal to L^* . For $L_d \leq L^*$ the measured temperature dependence of L_d is compatible with the form (16) (straight lines in Fig. 13) implying

$$A_d = \begin{Bmatrix} 84 \pm 43 \text{ \AA} \\ 37 \pm 8 \text{ \AA} \\ 42 \pm 9 \text{ \AA} \end{Bmatrix} \text{ and } T_s = \begin{Bmatrix} -13.5 \pm 2.6^\circ\text{C} \\ -12.8 \pm 1.9^\circ\text{C} \\ -12.4 \pm 1.9^\circ\text{C} \end{Bmatrix} \quad (18)$$

for $\begin{Bmatrix} \{00.1\} \\ \{10.0\} \dots \text{surfaces} \\ \{11.0\} \end{Bmatrix}$.

Since, as discussed before, the investigated nonbasal surfaces do not show any significant diffuseness of the solid–quasiliquid interface, we have to conclude that the observed growth amplitude $A_d \cong 40 \text{ \AA}$ must be identified with the relevant correlation length ξ_{qu} of the undercooled quasiliquid. Evidently it is much larger than the correlation in the bulk liquid (water), $\xi_b \cong 8 \text{ \AA}$, even when undercooling is taken into account [4,35]. Our finding, that the “surface melt” is much more correlated than the bulk melt, seems to reflect the action of the underlying “substrate” interactions which try to impose solid Fourier components onto the mesoscopic surface layer. Since these short ranged solid correlations decay exponentially within the quasiliquid on a length scale comparable to ξ_{qu} , it is not unreasonable that the average density of the mesoscopic disordered surface sheet is still close to that of the solid as long as $L_d \leq 100 \text{ \AA}$. This would provide a natural explanation for the fact that ellipsometry measurements pick up liquid surface signals only very closely to the bulk melting point. Actually, ellipsometry measurements at basal surfaces detect a changed index of refraction at $T = -2^\circ\text{C}$ [13], thus, almost at the temperature associated with L^* , where we observe a crossover to a strongly enhanced surface melting (see Fig. 13). Another interesting property of the quasiliquid layer may directly be related to the enhanced correlation length: As detected by NMR measurements on ice surfaces [36] the diffusion constant within the quasiliquid is distinctly reduced by 4 orders of mag-

nitude compared to bulk water. Similar results have also been obtained by quasielastic light scattering from the interfacial region between water and ice during crystal growth [37]. This slowing down phenomenon is well known in bulk critical systems and is identified to be caused by a strongly enhanced (there actually diverging) correlation length.

This substrate-induced enhancement of the correlation length within the surface melt should also be present at basal surfaces, however, the large growth amplitude $A_d \cong 84 \text{ \AA}$ is most likely affected by the strongly fluctuating solid-quasiliquid interface, implying $A_d \sim (T/\gamma_{sl})^{1/2}$ (as discussed above). Since γ_{sl} is very small, the growth of this surface layer may be further enhanced. This scenario implies a slightly temperature-dependent growth amplitude, therefore, the deduced value $A_d = 84 \pm_{14}^{43} \text{ \AA}$ should hold only approximately. Interestingly, in this case, also the interfacial roughness ρ_{sl} is predicted to depend on temperature [31],

$$\rho_{sl} \sim \{\ln(T_m - T)\}^{1/2}. \quad (19)$$

This relation has been tested in Fig. 14 and turns out to be perfectly compatible with our measured values. This gives additional evidence for the existence of a fluctuating solid-quasiliquid interface, however, we emphasize once more that ρ_{sl} has not been proven to be reversible with temperature (see Fig. 8c).

Two other aspects related with surface melting of

ice are noteworthy, because, in principle, they also can cause an enhanced growth amplitude and an effective surface waviness. They can be excluded to play a role, though, under the experimental conditions of this study:

(a) Löwen and Lipowsky [38] argued that surface melting under the condition of undersaturation leaves the $\ln |T_m - T|$ -law essentially intact, but gives rise to a renormalized growth amplitude $A_d^* = A_d(1 + \dot{S}/v_D)$ with v_D as the typical diffusion-limited velocity in the system, i.e. $v_D \cong D_{qli}/\xi_{qli}$. The numerical values $D_{qli} \cong 10^{-8} \text{ cm}^2/\text{s}$ (from Ref. [36]) and $\xi_{qli} \cong 50 \text{ \AA}$ (as deduced from this study) imply that v_D is of the order of some $\mu\text{m/s}$ and consequently $\dot{S}/v_D = 10^{-3}$ in our case, i.e. still negligibly small.

(b) Recently, the influence of van der Waals interactions upon the surface melting of ice has been analyzed in view of the aforementioned crossover of the UV dielectric function between ice and water causing a sign change of the Hamaker constant [39]. At $L_d \cong 30 \text{ \AA}$ the growth of the quasiliquid should stop ("blocked surface melting") and any vapour condensation at the surface should form nonequilibrium water droplets with a shallow contact angle around 0.2° . Since our experiments have always been performed in the undersaturation regime, such droplet formation which would indeed give rise to an effectively wavy surface horizon can safely be ruled out.

In fact, our experiments do not confirm the predicted blocked surface melting at $L_d = 30 \text{ \AA}$ [39]. Apparently, the enhanced correlation length dominating the quasiliquid extends the action of the exponentially decaying interactions way beyond this blocking thickness of 30 \AA . According to our results van der Waals interactions start to noticeably dominate the surface melting scenario not before the thickness of the quasiliquid layer exceeds the critical thickness $L^* \cong 150 \text{ \AA}$. It is quite remarkable that our X-ray results for the temperature-dependent thickness of the quasiliquid are not too far from relation (1) as deduced by Fletcher [6] from rather straightforward electrostatic arguments. One may thus speculate whether local electric fields near the ice surface play a major role for the surface melting process (recent MD simulations also suggest that such near surfaces fields affect TIP4P ice quite significantly [40]). The apparent discrepancies between our X-ray observations and the two theoretical surface melting

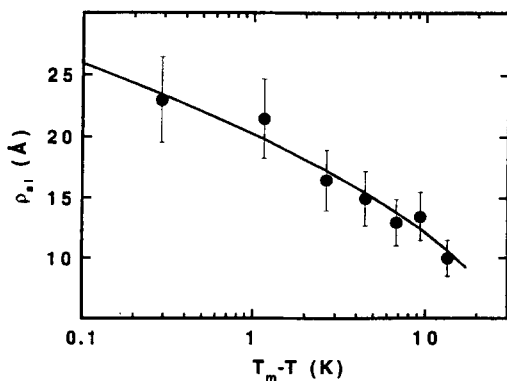


Fig. 14. Roughness ρ_{sv} (and ρ_{sl} for $T > -13.5^\circ\text{C}$, respectively) at the {00.1} surface versus $\ln |T_m - T|$. The full line represents the relation (19).

scenarios described in Ref. [6] and [39] are certainly in part due to the fact that both theoretical approaches describe the emerging liquid surface layer essentially with bulk liquid properties (in particular regarding its dielectric behaviour), while the X-ray evidence suggests the presence of a much stronger correlated undercooled quasiliquid which has a polarizability presumably much closer to ice than to water. We also want to mention that we did not find a noticeable signature of a roughening transition at prism surfaces proposed to occur at $T = -1.35^\circ\text{C}$ [41], nonetheless, around $T \approx -1.0^\circ\text{C}$ a strong increase of the thickness of the disordered surface appears (see Fig. 11c) which may be related with the optical observations reported in Ref. [41]. Since the relevant interaction in H_2O is mediated by the hydrogen-bonding network, some surface-induced disorder in the hydrogen long range order has to accompany or even induce the ice surface melting. In recent X-ray experiments performed at prism surfaces of ice the pure hydrogen X-ray scattering has been isolated and analyzed at various temperatures. The obtained surface-dominated diffraction profiles do strongly support this idea. This will be published in a forthcoming paper [42].

Acknowledgements

We are grateful to the HASYLAB administration for continuous support of the ice project and to the local HASYLAB staff for technical assistance during our measurements. We thank H. Peisl for his support. This work was funded by the Bundesminister für Forschung und Technologie (BMFT) under Grants No. 03PE1LMU and No. 03PE1LMU2.

References

- [1] J.G. Dash, H. Fu and J.S. Wettlaufer, Rep. Prog. Phys., to appear.
- [2] M. Faraday, Philos. Mag. 17 (1859) 162.
- [3] A. Lied, H. Dosch and J.H. Bilgram, Phys. Rev. Lett. 72 (1994) 3554.
- [4] A.H. Narten and H.A. Levy, in: Water a Comprehensive Treatise 1: The Physics and Physical Chemistry of Water, Ed. F. Franks (Plenum, New York, 1972).
- [5] N.H. Fletcher, Philos. Mag. 7 (1962) 255.
- [6] N.H. Fletcher, Philos. Mag. 18, (1968) 1287.
- [7] J.W. Telford and J.S. Turner, Philos. Mag. 8 (1963) 527.
- [8] H.H.G. Jellinek, Can. J. Phys. 40 (1962) 797.
- [9] C. Jaccard, in: Physics of Snow and Ice, Ed. H. Oura (Hokkaido University, Sapporo, 1967).
- [10] D. Nason and N.H. Fletcher, J. Chem. Phys. 62 (1975) 4444.
- [11] I. Golecki and C. Jaccard, J. Phys. C 11 (1978) 4229.
- [12] D. Beaglehole and D. Nason, Surf. Sci. 96 (1980) 357.
- [13] Y. Furukawa, M. Yamamoto and T. Kuroda, J. Cryst. Growth 125 (1987) 665.
- [14] M. Elbaum, Phys. Rev. Lett. 67 (1991) 2982.
- [15] T. Kuroda and R. Lacmann, J. Cryst. Growth 56 (1982) 189.
- [16] S.C. Colbeck, J. Cryst. Growth 72 (1985) 726.
- [17] A. Lied, H. Dosch and J.H. Bilgram, Physica B 198 (1994) 92.
- [18] H. Dosch, Vol. 126 of Springer Tracts in Modern Physics (Springer, Berlin, 1992).
- [19] H. Dosch, Int. J. Mod. Phys. B 6 (1992) 2773.
- [20] S. Dietrich and H. Wagner, Z. Phys. B 56 (1984) 207.
- [21] H. Dosch, B.W. Batterman and D.C. Wack, Phys. Rev. Lett. 56 (1986) 1144.
- [22] H. Dosch, Phys. Rev. B 35 (1987) 2137.
- [23] S.K. Sinha, E.B. Sirota, S. Garoff and H.B. Stanley, Phys. Rev. B 38 (1988) 2267.
- [24] J.H. Bilgram, H. Wenzl and G. Mair, J. Cryst. Growth 20 (1973) 319.
- [25] J. Muguruma, J. Phys. D 2 (1969) 1517.
- [26] E. Beckmann and R. Lacman, J. Cryst. Growth 58 (1982) 433.
- [27] M. Pavalow and A. Zajac, Physics and Chemistry of Ice, Eds. E. Whalley, S.J. Jones and L.W. Gold (Royal Society of Canada, Ottawa, 1973).
- [28] A. Goto, K. Akija, T. Hondoh, Y. Furukawa, T. Shimura, I. Takahashi and J. Harada, J. Cryst. Growth 121 (1992) 360.
- [29] J.D. Cross, in: Physics of Ice, Eds. N. Riehl, B. Bullemer and H. Engelhardt (Plenum, New York, 1969).
- [30] D.G. Vlachos and D. Schmidt, R. Aris, Phys. Rev. B 47 (1992) 4896.
- [31] R. Lipowsky, Ferroelectrics 73 (1987) 69.
- [32] J.W.M. Frenken and J.F. van der Veen, Phys. Rev. Lett. 54 (1985) 134;
for a review see: J.F. van der Veen, B. Pluis and A.W. Denier van der Gon, in: Chemistry and Physics of Solid Surfaces, Vol. VII; Eds. R. Vanselow and R.F. Howe (Springer Berlin, 1988).
- [33] Note that Eq. (16) follows from an effective interface potential $V(L) = aL + b \exp(L/A_d)$, where A_d is an arbitrary model-dependent length scale. Quite generally, $A_d = \xi_d$, where ξ_d is the leading length scale in the problem, either mediated by the correlations within the liquid phase or/and by the underlying substrate. (Within mean field theory applied in Ref. [31] A_d is given by the correlation length ξ_b associated with the liquid phase.)
- [34] I.E. Dzyaloshinskii, E.M. Lifshitz and L.P. Pitaevskii, Adv. Phys. 10 (1961) 165.

- [35] Y. Xie and K. Ludwig, Jr., Phys. Rev. Lett 71 (1993) 2050.
- [36] Y. Mizumo and N. Hanafusa, J. Phys. Coll. 48 (1981) C1.
- [37] P. Böni, J.H. Bilgram and W. Känzig, Phys. Rev. A 28 (1983) 2953.
- [38] H. Löwen and R. Lipowsky, Phys. Rev. B 43 (1991) 3507.
- [39] M. Elbaum and M. Schick, Phys. Rev. Lett. 66 (1991) 1713.
- [40] I.G. Svishchev and P.G. Kusalik, Phys. Rev. Lett. 73 (1994) 975.
- [41] M. Elbaum, S.G. Lipson and J.G. Dash, J. Cryst. Growth 129 (1993) 491.
- [42] H. Dosch, A. Lied and J.H. Bilgram, to be published.